Geophysical Journal International

Geophys. J. Int. (2024) **237,** 916–930
Advance Access publication 2024 March 1
GJI Seismology

https://doi.org/10.1093/gji/ggae077

AI based 1-D *P*- and *S*-wave velocity models for the greater alpine region from local earthquake data

Benedikt Braszus,[1] Andreas Rietbrock,[1] Christian Haberland[2] and Trond Ryberg[2]

[1]*Karlsruhe Institute of Technology, Geophysical Institute, 76187 Karlsruhe, Germany. E-mail: benedikt.braszus@kit.edu*
[2]*GFZ German Research Centre for Geosciences, 14473 Potsdam, Germany*

Accepted 2024 February 29. Received 2023 October 10; in original form 2024 February 2

SUMMARY

The recent rapid improvement of machine learning techniques had a large impact on the way seismological data can be processed. During the last years several machine learning algorithms determining seismic onset times have been published facilitating the automatic picking of large data sets. Here we apply the deep neural network *PhaseNet* to a network of over 900 permanent and temporal broad-band stations that were deployed as part of the AlpArray research initiative in the Greater Alpine Region (GAR) during 2016–2020. We selected 384 well distributed earthquakes with $M_L \geq 2.5$ for our study and developed a purely data-driven pre-inversion pick selection method to consistently remove outliers from the automatic pick catalogue. This allows us to include observations throughout the crustal triplication zone resulting in 39 599 *P* and 13 188 *S* observations. Using the established VELEST and the recently developed McMC codes we invert for the 1-D *P*- and *S*-wave velocity structure including station correction terms while simultaneously relocating the events. As a result we present two separate models differing in the maximum included observation distance and therefore their suggested usage. The model *AlpsLocPS* is based on arrivals from $\leq$130 km and therefore should be used to consistently (re)locate seismicity based on *P* and *S* observations. The model *GAR1D_PS* includes the entire observable distance range of up to 1000 km and for the first time provides consistent *P*- and *S*-phase synthetic traveltimes for the entire Alpine orogen. Comparing our relocated seismicity with hypocentral parameters from other studies in the area we quantify the absolute horizontal and vertical accuracy of event locations as ≈2.0 and ≈6.0 km, respectively.

Key words: Machine learning; Body waves; Crustal imaging; Seismicity and tectonics.

1 INTRODUCTION

While the underlying cause for the Alpine orogeny can be attributed to the collision of the Eurasian and African continental plates, the complex interactions and reorganizations of wedged microplates such as the Adriatic Plate is yet not fully understood (Schmid *et al.* 2004; Handy *et al.* 2010).

This collision did not only form the present day surface topography of the orogen but also caused the formation of a crustal root beneath the mountain belt leading to strong variations in Moho depths ranging from 20 to 25 km in the Northern and Northwestern foreland to 50–55 km beneath the Central and Western Alps (Spada *et al.* 2012). The European *AlpArray* research initiative (AlpArray Seismic Network 2015) aims to gain novel insights into the Alpine orogeny in space and time. The central part of this interdisciplinary and international project (involving 36 institutions from 11 countries) was to densify the existing permanent seismic networks by the temporary AlpArray Seismic Network (Hetényi *et al.* 2018). Additional networks with a more local focus such as the SWATH-D (Heit *et al.* 2021) were also deployed to study in high resolution specific aspects of the Alpine orogeny. Based on this unprecedented data set a wide range of seismological methods was applied to sharpen our understanding of plate/microplate reorganization, mantle dynamics and their relation to surface processes.

Recent studies have leveraged the AlpArray data set to (re)-assess seismicity as well as to refine the *P* and *S* wave 1-D and 3-D velocity structure in the Greater Alpine Region (GAR). Recently, a comprehensive analysis of the seismicity in the entire GAR between 2016 and 2019 has been conducted by Bagagli *et al*. (2022). They used observations from distances of up to of 300 km to invert for a 1-D *P*-wave velocity model and hypocentral parameters with the well-established VELEST code (Kissling *et al.* 1994). On a more local scale Jozi Najafabadi *et al.* (2021) inverted *P* and *S* phases with epicentral distances of up to 160 km for a 1-D velocity model resolving the upper and mid crust beneath the Central Eastern Alps using an Markov chain Monte Carlo (McMC) algorithm from Ryberg & Haberland (2019). Using data from the Swiss seismic network Diehl *et al.* (2021) published a local 3-D *P*- and *S*-wave velocity model

for the broader Swiss region. Complimentary, ambient noise studies obtaining 3-D crustal and upper mantle *S*-wave velocity models of the GAR have been conducted by Kästle *et al.* (2018) and Sadeghi Bagherabadi *et al.* (2021).

In this study, we invert traveltime observations from the 384 events and 958 seismic stations displayed in Fig. 1 in order to obtain for the first time a joined 1-D *P*- and *S*-wave velocity model for the GAR including station correction terms while simultaneously relocating the seismicity. A very basic task inherent to earthquake location and seismological tomographic studies is the determination of seismic phase arrival times. Considering the huge amount of waveforms available nowadays the application of automatic picking tool is indispensable. Accompanied by the recent rapid advances in research and application of artificial intelligence in general several deep neural network based seismic picking algorithms have been developed. They were found to reach the level of accuracy of human analysts (Weiqiang & Beroza 2018; Woollam *et al.* 2019) and have been used for various seismological task such as monitoring of volcanoes (Lapins *et al.* 2021) and real-time analysis of seismograms (Kuang *et al.* 2021; Münchmeyer *et al.* 2021). We carefully assess the performance of the most widely used neural network pickers on our data set using *Seisbench—A toolbox for machine learning in seismology* based on Woollam *et al.* (2022) and Münchmeyer *et al.* (2022).

For the inversion we apply the McMC and VELEST algorithms to our *P*- and *S*-phase data and as a result present the first orogen wide traveltime based 1-D *P*- and *S*-wave model of the GAR. Our *AlpsLocPS* model with resolution in the upper and mid crust is based on observations from distances of 0–130 km and allows consistent (re)localization of seismicity within the GAR using *P* and *S* phases. The *GAR1D_PS* model incorporates arrivals from up to 1000 km and therefore resolves the entire crust and the uppermost mantle.

2 DATA

The majority of waveforms analysed is provided by the AlpArray seismic network (Hetényi *et al.* 2018) which has been in operation from 2015 to 2021 as part of the European interdisciplinary AlpArray Research initiative. Due to a hexagonal packing strategy, the partially heterogeneous distribution of permanent broad-band stations in the GAR could be effectively densified to a maximum station spacing of 52 km. Thus, each point within the GAR is located within a 30 km radius of a seismic broad-band station. Additionally, from October 2017 until September 2019 the SWATH-D network improved the station spacing in the Eastern and Southern Alps to 15 km (Heit *et al.* 2021).

We used the FDSN client implemented in ObsPy (Krischer *et al.* 2015) to collect station metadata and seismic broad-band waveform data from 958 stations in the GAR between the years of 2016 and 2020. Only data with a sampling rate of at least 100 Hz and a channel of either 'HH?', 'BH?' or 'EH?' has been considered. We do not remove the instrument response during processing. For consistency reasons, we resample all data to *PhaseNet's* (Weiqiang & Beroza 2018) required sampling rate of 100 Hz before feeding the waveforms to several deep learning picking algorithms. Event detections with $M_L \geq 2.5$ and corresponding initial hypocentral parameters are obtained from the European–Mediterranean Seismic Centre (EPOS-EMSC)(*https://www.seismicportal.eu/*). The used 958 stations and 384 events are shown in Fig. 1 as red triangles and blue circles, respectively.

3 METHODS

3.1 Phase picking

3.1.1 Evaluation of neural network picking algorithms using Seisbench

The recent rapid improvement of machine learning techniques had a strong impact on seismic data analysis. We utilize this development by testing the performance of the most widely used neural network picking algorithms on our seismic waveform data. With the recently published Seismology Benchmark collection *SeisBench* (Woollam *et al.* 2022) we applied the deep-neural-network picking algorithms *PhaseNet* (Weiqiang & Beroza 2018), *EarthquakeTransformer* (EQT; Mousavi *et al.* 2020) and *GPD* (Ross *et al.* 2018) to waveforms recorded in the Swiss Alpine region for which a high quality manual reference pick catalogue from Diehl *et al.* (2009a) was available. This catalogue consists of 1801 *P*-phase picks recorded from 1997 to 2006 and was compiled for a local earthquake tomography study of the greater Swiss area (Diehl *et al.* 2009a).

The neural network pickers are built on different architectures and were trained on distinct training data sets yielding one final model per architecture and training data pair. Seisbench incorporates several models for each picker based on different training data such as the ETHZ (SED at ETH Zurich 1983), SCEDC (SCEDC 2013), NCEDC (NCEDC 2013), INSTANCE (Michelini *et al.* 2021) and STEAD (Mousavi *et al.* 2019) data sets. In order to assess the pickers' performance we compared the picks obtained by each neural network to the high quality manually picked catalogue of phase arrival times and associated quality classes.

The performance of the picking algorithms is assessed by the mean offset μ, the standard deviation σ and recall of the neural network picks with regard to the manual catalogue. These parameters are compared in Table 1 for the tested combinations of network architectures and training data sets.

Although μ and σ are only varying moderately between the different automatic pickers, the recall, defined as the percentage of retrieved picks from the reference data, fluctuates significantly. This parameter strongly depends on the user-defined probability threshold t_{prob}. The lower the threshold, the higher the number of picks is in general and therefore increases the recall but at the same time causes more erroneous picks.

We decided to use the neural network *PhaseNet* in its original configuration, that is $t_{\text{prob}} = 0.3$, trained on the *NCEDC* data set for all further analysis, since its higher recall in our opinion outweighs the slightly increased mean offset μ.

Fig. A1 shows a comparison of 1702 matching picks from Diehl *et al.* (2009a) and *PhaseNet*. As the mean offset of $\mu = 0.15$ s indicates, the entire distribution is slightly shifted to negative values, that is late *PhaseNet* picks. Furthermore, it can be observed that the number of outliers with $|\Delta_t| > 1.0$ s is significantly larger for negative values. Late *PhaseNet* picks predominantly occur in the distance range of ≈100–300 km coinciding well with the crustal cross-over distance of *Pg*, *PmP* and *Pn* phases where *PhaseNet* is not able to always pick the rather small amplitude *Pn* first arrival. In Section 3.4, we present a purely data-driven approach to consistently remove the overcritical *Pg*/*Sg* picks while minimizing the number of discarded first arrival observations.

Seismicity in the GAR is mainly limited to the upper crust with few exceptions (Bagagli *et al.* 2022). This generally causes a rather pronounced appearance of the crustal *Pg*, *PmP* and *Pn* phases and

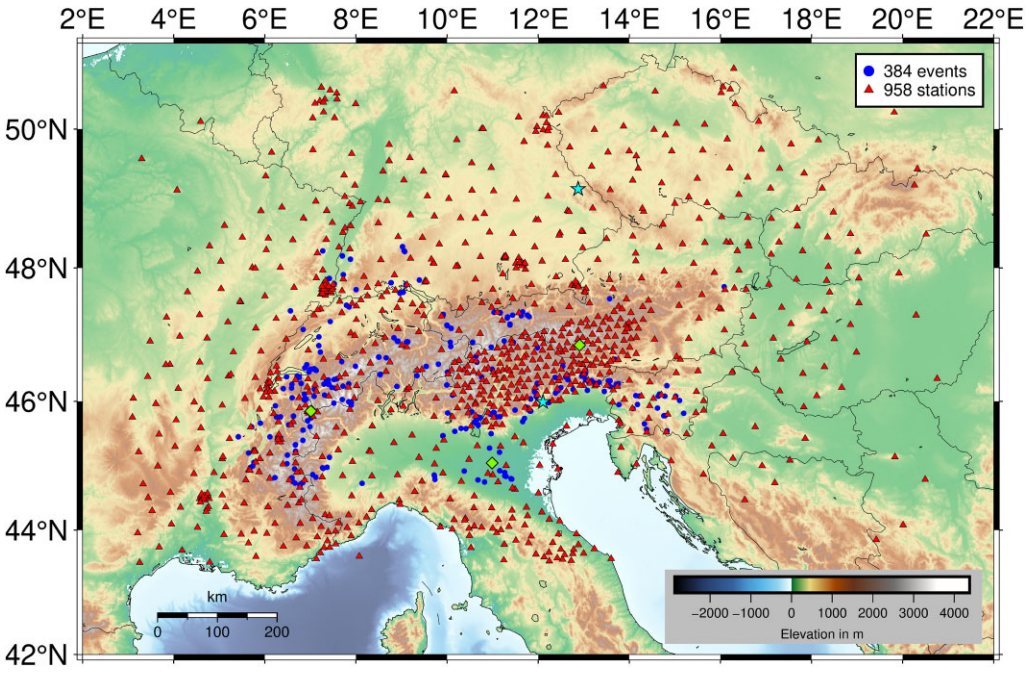

Figure 1. Overview map of the Greater Alpine region showing locations of the 958 broad-band seismic stations (red triangles) and 384 events (blue dots) with $M_L \geq 2.5$ used in this study. Purple dots are showing the seismicity of the *AlpArray Research Seismicity-Catalogue* from Bagagli *et al.* (2022). Stations *VARN* (NE Italy) and *WETR* (SE Germany) referred to in Fig. 9 are highlighted with cyan stars, locations at which 1-D v_s profiles (Fig. 11) are extracted from the 3-D *S*-wave models from Kästle *et al.* (2018) and Sadeghi Bagherabadi *et al.* (2021) are marked with light green diamonds.

Table 1. Table assessing the performance based on mean μ, standard deviation σ and recall of several neural network picking algorithms trained on various benchmark data sets using *Seisbench* (Woollam *et al.* 2022) when compared to the manual *P*-phase pick catalogue from Diehl *et al.* (2009a).

Neural network	Training data	μ (s)	σ (s)	Recall (per cent)
PhaseNet	NCEDC (org)	−0.15	0.27	95
	ETHZ	−0.07	0.30	80
	STEAD	−0.12	0.28	64
	INSTANCE	0.02	0.37	90
EQT	INSTANCE	−0.12	0.26	80
	ETHZ	−0.05	0.27	79
	STEAD	−0.09	0.19	35
	SCEDC	−0.08	0.26	55
	Original	−0.09	0.26	36
GPD	ETHZ	−0.13	0.24	91
	STEAD	−0.1	0.22	92
	SCEDC	−0.09	0.17	67

thus creates a more complex wavefield than in, for example a subduction zone setting.

3.1.2 PhaseNet versus manual picks

As a next step we further verify the applicability of *PhaseNet* to our data set and compare its accuracy against the inevitable influence of human subjectivity when manually determining phase arrival times. Therefore, a human analyst picked *P*- and *S*-phases from 30 events with epicentres in the Central Alpine area recorded in 2018. Six of these events were picked by a second analyst to exemplarily validate the picking accuracy. Values of μ and σ are not deviating significantly between both comparisons (see Fig. A2) supporting the conclusion that *PhaseNet*'s picks are almost as accurate and consistent as manually determined onset times. Generally, the *S*-phase discrepancies are slightly higher most likely due to the less impulsive onset within the *P*-phase coda. When comparing *PhaseNet* and manual picks over several epicentral distance ranges we observe an increase of the standard deviation with distance for picks observed between 0 and 300 km (Figs A3a–c) and no further increase in deviation for picks from distances ≥300 km (Fig. A3d).

Finally, we compare *PhaseNet* to a set of manually revised picks from Jozi Najafabadi *et al.* (2021) comprising 16 events from the Central Alps within the boundaries of the SWATH-D network (see Fig. A4). *P*- and *S*-phase inconsistencies are very similar to the values from Table 1 and Fig. A2.

3.2 Development of a weighting scheme based on *PhaseNet*'s pick probability

Most earthquake location and inversion algorithms allow the assignment of an uncertainty value or weight to each individual phase arrival in order to increase the impact of accurate picks on the inversion result. The importance of a consistent weighting of picks based on their accuracy and the influence on the resulting tomographic image has been demonstrated by Diehl *et al.* (2009b). Even though *PhaseNet* does not output the uncertainty of the preferred onset time, if run in default mode it outputs a probability between 0.3 and 1.0 for each pick. Thus, in order to assign a weight to each automatic pick we investigated the correlation between the *PhaseNet* probability and manually determined pick qualities based on the 1702 matching manual reference picks from Diehl *et al.* (2009a). Fig. 2 shows the deviations of manual and *PhaseNet* picks when clustering *PhaseNet* picks to the probability ranges 0.3–0.6, 0.6–0.75, 0.75–0.9 and 0.9–1.0. Picks with higher probabilities deviate

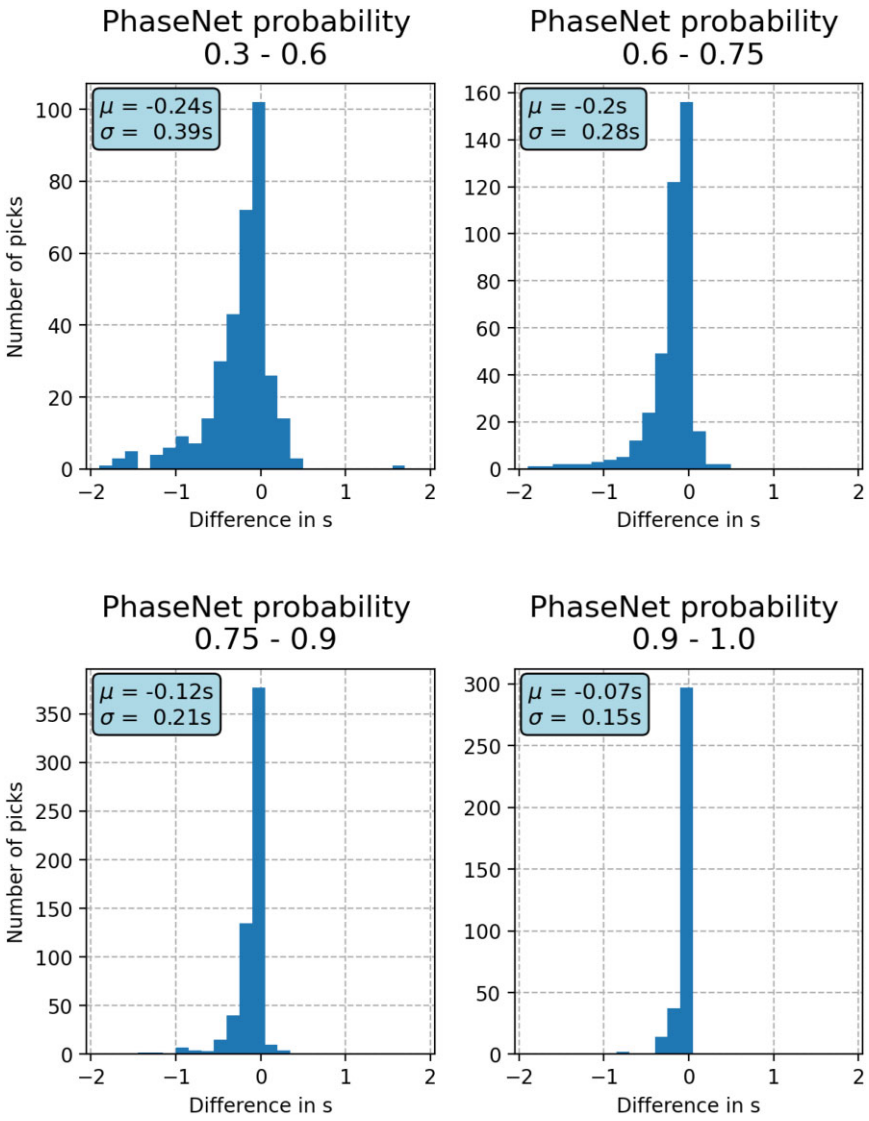

Figure 2. Difference in determined *P*-phase onset time between the high precision manual pick catalogue from Diehl *et al.* (2009a) and *PhaseNet*'s picks. Each panel corresponds to *PhaseNet* picks within the specified probability range.

significantly less from the manual reference pick indicating a correlation between probability and accuracy of the *PhaseNet* picks. Diehl *et al.* (2009a) assigned the classes 0, 1, 2, 3 and 4 corresponding to absolute pick uncertainties of 0.05, 0.1, 0.2, 0.4 and $>$0.4 s to each of their picks. Fig. 3 shows the number of picks per class for the same *PhaseNet* probability ranges as above. The most accurate manual picks predominately show up in the highest *PhaseNet* probability range, while lower class manual picks are more likely to fall into lower probability ranges. We use this correlation to estimate an average pick uncertainty ϵ. For each probability range the uncertainties associated to the manual pick classes 0–3 are averaged while weighted by the number of corresponding picks. Class 4 picks are not considered since they were not assigned a discrete uncertainty value. Even though the absolute values of ϵ seem to be an underestimation of the actual uncertainty when compared to the values of μ and σ in Fig. 2, the trend of increasing accuracy with increasing pick probability is systematic which suggests relative weighting of *PhaseNet* picks based on their probability.

3.3 Event section plot

As an illustrative way to display the vast amount of seismic data available for this study we show an event section plot of a $M_L = 3.8$ event in NE Italy in Fig. 4(a). The trace normalized vertical components are shown over their epicentral distance. The traveltime on the *y*-axis is corrected with the approximate upper-crustal *P*-wave velocity of $v_p = 6.0\,\mathrm{km\,s^{-1}}$, so that the arrival of the direct *Pg* wave is aligned horizontally. Synthetic onset times are computed with *NonLinLoc* (Lomax *et al.* 2000) based on the 1-D *P*-wave velocity model from Diehl *et al.* (2009a) and a constant v_p/v_s ratio of 1.73 and indicated with purple and pink horizontal bars for *P* and *S* phases, respectively. Although *PhaseNet*'s *P*-phase picks as selected or discarded by the *2-fit method* (Section 3.4) are shown in red and blue, respectively. *S*-phase picks are plotted in green (selected) and orange (discarded), accordingly. At distances from ≈200 to 450 km *PhaseNet* also frequently picks the later arriving direct *Pg*-phase that is often misidentified as an incoming *S*-phase (orange) possibly due to its shallow incidence angle. Similarly, the *Sn*-phase

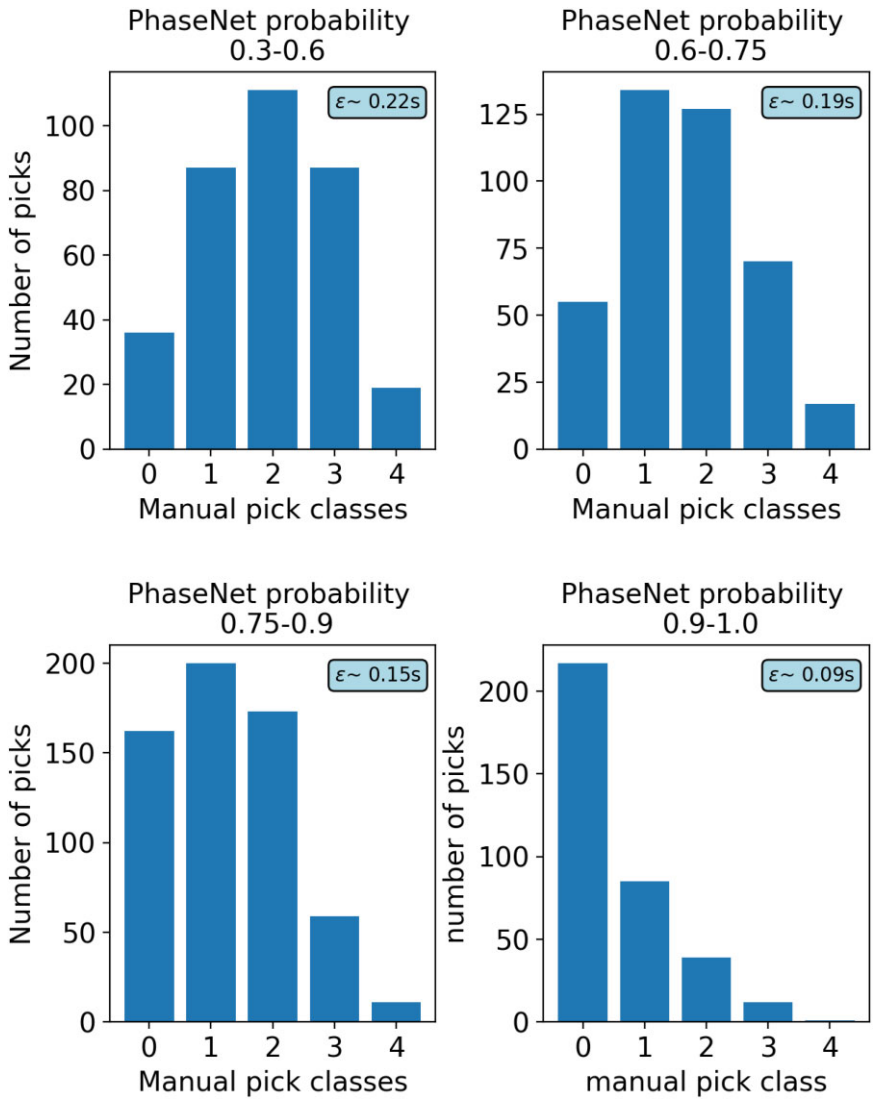

Figure 3. Number of manually assigned pick classes for *P* phases in Diehl *et al.* (2009a) for the four given *PhaseNet* probability ranges. The error estimate ϵ averages the accuracy values from 0.05 to 0.4 s as assigned to each pick class in Diehl *et al.* (2009a) weighted by their occurrence in the corresponding probability range.

often seems to be mislabelled as a *P* phase. Therefore, when applying the *2-fit-method* we are considering all *PhaseNet* picks at distances $\geq$200 km within $\pm$7 s of the synthetic *S*-phase onset to be *Sn* phases regardless of their *PhaseNet* label. Those manually relabelled onsets are indicated by green circles with red edgecolour in Fig. 4(a).

3.4 Selection of a reliable data subset

The task of identifying and removing outliers in the data is of increased importance when dealing with an automatically picked catalogue of arrival times usually containing more erroneous picks than manually picked data. In principle, this can be approached from the model as well as from the data side. Selecting outliers based on the model requires detailed *a priori* information of the region in order to remove picks based on their residual with respect to a certain reference model. Here, one has to be careful to not simply select picks that confirm the initial assumptions and discard data that contains valuable true signal, but deviates from the reference model.

To mitigate such a model anchoring, we developed a purely data driven approach. Fig. 4(b) illustrates our new '*2-fit-method*' applied to *P*-phase arrivals from the same event as in Fig. 4(a). Phase onsets are plotted over epicentral distance with their reduced traveltime $v_{red} = 8.0\,km\,s^{-1}$. Blue crosses mark the synthetic arrival time based on the 1-D model from Diehl *et al.* (2009a) and green crosses draw a $\pm$7 s corridor around them. Since all picks outside of this corridor are discarded it has to be wider than the maximum expected signal amplitude. Initially, a weighted linear regression is fit through arrivals from 0 to 100 km and extrapolated. Picks within the blue corridor at distances $\geq$150 km within 4σ of this extrapolation are discarded as overcritical *Pg* phases (cyan). Later arrivals (purple) are discarded as potential *PmP* phases. Another weighted regression is fit through the remaining data between 250 and 700 km and extrapolated in both directions until it intersects the first fit for the direct arrivals. All arrivals within 2σ of these two regressions

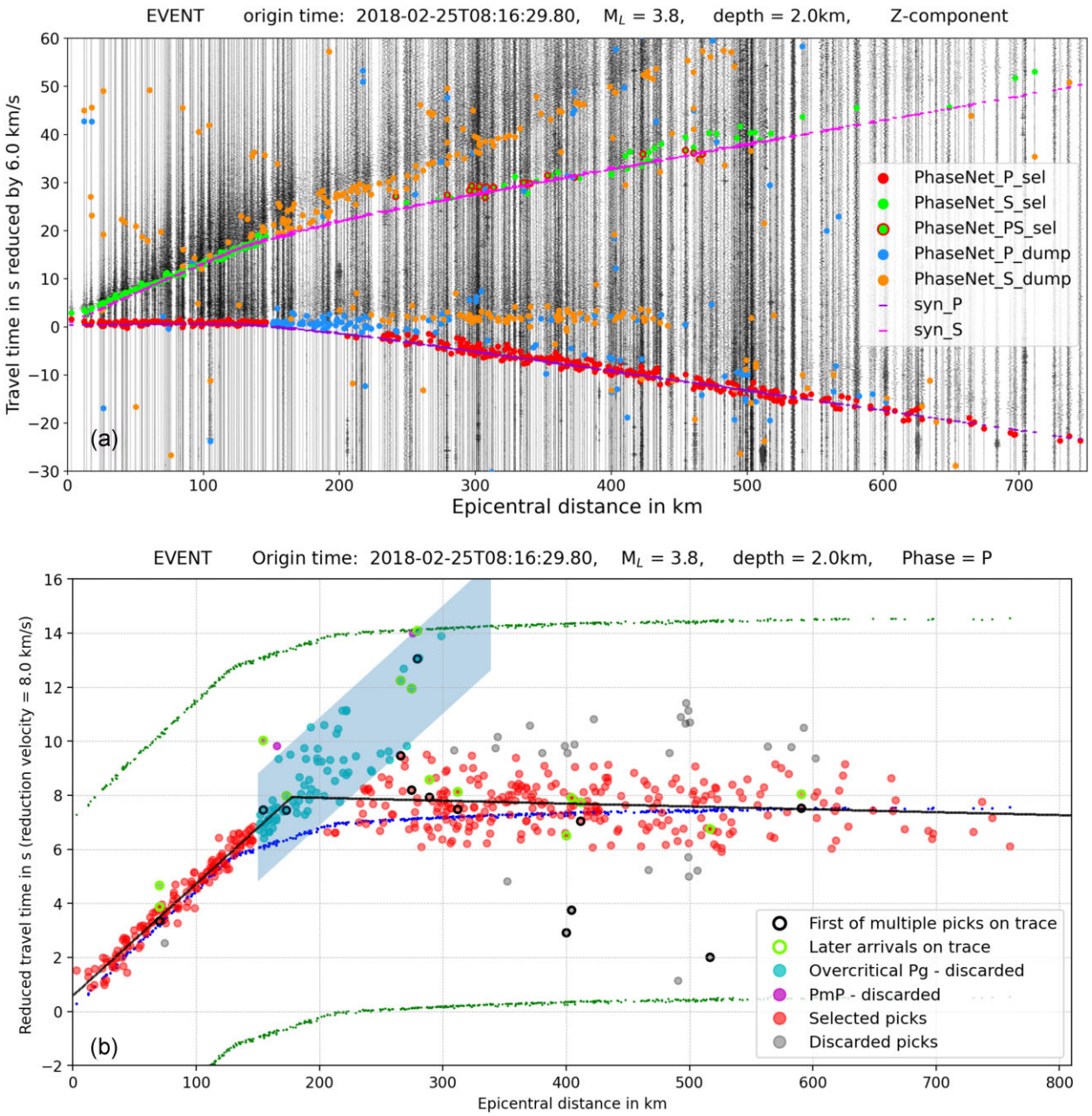

Figure 4. (a) Event section plot showing the normalized traces of vertical components over their epicentral distance for a $M_L = 3.8$ event at 2.0 km depth in NE Italy. The traveltimes on the *y*-axes are corrected with the approximate upper-crust *P*-wave velocity of $v_p = 6.0\,\mathrm{km\,s^{-1}}$. Synthetic onset times based on the 1-D *P*-wave velocity model from Diehl *et al.* (2009a) and a constant v_p/v_s ratio of 1.73 are marked with purple and pink horizontal bars for *P* and *S* phases, respectively. *PhaseNet P*- and *S*-phase picks selected by the *2-fit method* are shown in red and green, while discarded *P*- and *S*-onsets are plotted in blue and orange, respectively. Green markers with red edgecolour are onsets that have been labelled as *P* phases by *PhaseNet*, but are considered to be *Sn* phases due to their proximity to the synthetic *S*-onset. (b) Illustration of the 2-fit method to discard erroneous picks. *PhaseNet P*-phase arrivals are plotted over epicentral distance with a reduction velocity of $8.0\,\mathrm{km\,s^{-1}}$. The corridor of considered picks is marked with green crosses at ± 7 s around the synthetic onset (blue crosses) based on the 1-D model from Diehl *et al.* (2009a). A linear regression is fit through the picks from 0 to 100 km and then extrapolated. All picks within the blue corridor at $\Delta \geq 150$ km within 4σ of this fit are labelled as overcritical *Pg* phases (cyan) and discarded. Later phases with $\Delta \geq 150$ km are discarded as *PmP* arrivals (purple). A second weighted linear regression is fit through arrivals from 250 to 700 km and extrapolated until its interjection point with the first fit. Arrivals within 2σ of the fits plotted in red are selected, while the remaining picks marked in grey are discarded. In the case of more than one arrival on the same trace, only the first arrival within 2σ of the fit is considered. First and later arrivals on the same trace are marked with black and lime edgecolours, respectively.

are selected for the inversion and marked with red circles, while the remaining picks plotted as grey circles are not considered for further processing. In the case of multiple picks per trace, only the first arrival within the 2σ range around the regression is selected. An example of this *'2-fit-method'* applied to *S*-arrivals is shown in Fig. A5.

This approach requires a rather linear moveout of the direct *Pg*/*Sg* wave which only is given for events shallower than

≈15 km. After manual inspection our *'2-fit-method'* yielded stable results for 384 events selecting a total of 39 599 *P* and 13 188 *S* observations.

Testing the *'2-fit-method'* on the reference data set from Diehl *et al.* (2009a) reduces $\mu = -0.15$ s to $\mu = -0.09$ s and $\sigma = 0.27$s to $\sigma = 0.15$ s when comparing the manual picks to the initial and the selected *PhaseNet* picks, respectively.

While the number of *Pg*-phases picked by *PhaseNet* (Fig. 4a) matches the number of manually pickable onsets (see Fig. A6) rather well, for all other phases the *PhaseNet* picks outnumber the manual ones. Out of all *PhaseNet* picks there are 410 *P* phases and 178 *S* phases selected, compared to the manual 286 *P* and 68 *S* onsets. Especially, the *Sn* onset could not be manually determined at all and has been consistently picked as the overcritical *Sg* phase, due to its low signal-to-noise ratio within the *P* coda, in particular between ≈150 and 280 km epicentral distance (see Fig. A6). The overcritical *Pg* and *Sg* phases are consistently picked by *PhaseNet* well beyond distances of 400 km. Since this study focuses purely on first arrivals we discarded them all. Nevertheless, they contain additional information that could be very valuable to studies incorporating secondary arrival picks.

3.5 Spatial distribution of initial residuals

A map view of the *P*- and *S*-phase residuals with respect to the 1-D model from Diehl *et al.* (2009a) for the same event as in Fig. 4 is shown in Fig. 5. Black dots mark station locations where waveforms were recorded but no phase onset within the corridor of ±7 s around the synthetic arrival time was detected by *PhaseNet*. Picks selected and discarded by the *2-fit-method* are marked as circles and diamonds, respectively. The map shows a rather smooth distribution of residuals with few contrasts between neighbouring stations. Overcritical *Pg*/*Sg* phases are mostly showing up as (dark)red circles and are consistently identified and discarded. Around the cross-over distance on the western edge of the SWATH-D network some picks might have been wrongly discarded since they appear reasonable when compared to residuals from neighbouring stations. This is acceptable, though, since the main objective of this step is to select a set of reliable picks.

3.6 Computation of minimum 1-D models with VELEST and McMC

We apply two different algorithms to simultaneously invert for a minimum 1-D *P*- and *S*-wave velocity model including station correction and hypocentral parameters from the selected seismic onset times. The VELEST (Kissling *et al.* 1994) code is well established for this task and requires an initial layered velocity model. While we use starting values for v_p from Diehl *et al.* (2009a) with slightly modified values in the upper mantle and an initial $v_p/v_s = 1.71$ based on an average of the model from Diehl *et al.* (2021), hypocentral parameters are taken from EPOS-EMSC. We tested ≈200 combinations for the three layer boundaries at depths between 15 and 45 km in order to find the parametrization with the best fit for our data and did not apply additional damping to individual layers. Since the inverse problem is linearized iteratively around the given initial parameters substantial *a priori* information is necessary.

Additionally, we apply the Bayesian McMC algorithm as initially developed by Ryberg & Haberland (2019). The McMC approach explores the entire discretized model space for each parameter and updates one single model parameter per iteration step. While models that lead to a reduced misfit are always accepted, models with increased misfit can be accepted as well with a low probability to overcome local minima.

As a result, the model will converge towards the global minimum of the objective function within the defined model boundaries. Eventually, a certain number *n* of the best-fitting models are statistically analysed to obtain uncertainty bounds for each model parameter based on its variance through the final set of well fitting models. Due to the so-called transdimensionality of the algorithm the number of model layers as well as the location of layer boundaries is optimized during the inversion yielding a smooth, gradient-like velocity model.

Since no initial model is given and the model boundaries are widely set to $2.0\,\mathrm{km\,s^{-1}} \leq v_p \leq 12.0\,\mathrm{km\,s^{-1}}$ and $1.0 \leq v_p/v_s \leq 2.5$ only minimum *a priori* information is implemented leading to a data-driven exploration of the entire reasonable model space.

The workflow towards the minimum 1-D models computed with VELEST and McMC is given in Table 2 and consists of three subsequent inversion runs.

The first run includes *P* and *S* phases with epicentral distances $\Delta \leq 130$ km for a spatially homogeneously distributed subset of 78 events in order to capture the average upper crustal *P*- and *S*-wave velocity structure without introducing a bias towards areas of increased seismicity and thus denser ray coverage. In the second run we compute the final locations for all 384 events by fixing the velocities from the first run and relocating all events using a total of 16 351 *P* and 10 967 *S* phases with $\Delta \leq 130$ km following Diehl *et al.* (2021) who showed a decrease of hypocentre accuracy when including distant observations for earthquake localization. During the third run we fix the event locations and additionally include 23 248 *P* and 2221 *S* observations with $\Delta \geq 130$ km in order to increase resolution in the lower crust and upper mantle. Station corrections and origin times are updated in each step and used as input for the subsequent run.

We perform one set of inversion runs with picks relatively weighted based on their *PhaseNet* probability and another one without weighting. There is no significant difference in the velocity structure and a standard deviation of $\sigma = 0.5$ km in the final epicentres with no systematic offset. Therefore, we decided to not include pick weights in our final models.

4 RESULTS

4.1 VELEST and McMC minimum 1-D models

Fig. 6 shows the 1-D v_p, v_p/v_s and v_s distribution of the *AlpsLocPS_McMC* (orange), *AlpsLocPS_VELEST* (red), *GAR1D_PS_McMC* (purple) and the 10 best-fitting (blue, dashed) as well as the final best-fitting (lime) *GAR1D_PS_VELEST* models.

In general the resulting *P*-wave velocity models (Fig. 6a) match quite well, except for the uppermost crust where both *AlpsLocPS* models exhibit increased values and the *GAR1D_PS_McMC* model shows a gradual velocity increase contrary to the *GAR1D_PS_VELEST* model. The large velocity jump at 32 km depth in the VELEST model is somewhat smoother in the McMC model, which still contains a rapid increase of v_p between 28 and 34 km depth. In this depth range the uncertainty in the *GAR1D_PS_McMC* model as well as the deviation of the 10 best-fitting *GAR1D_PS_VELEST* models is highest.

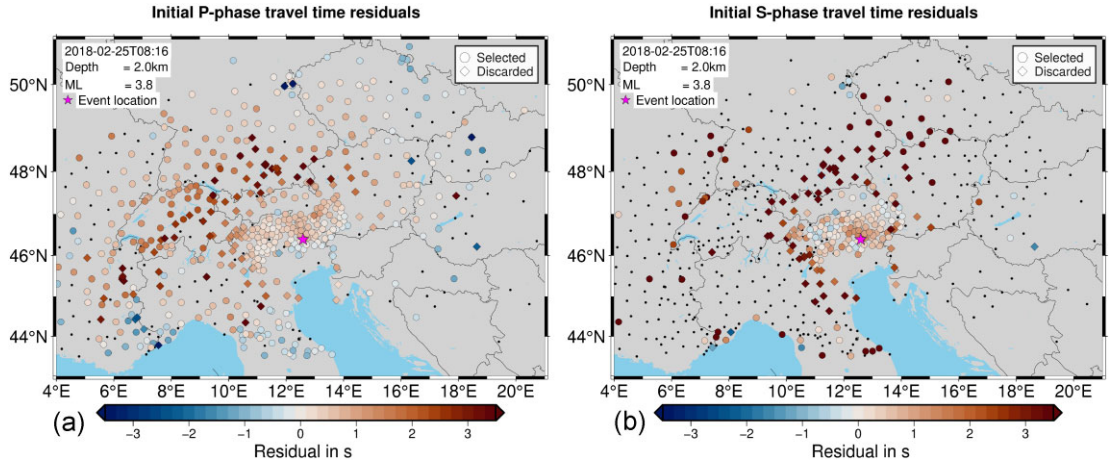

Figure 5. Initial *P*- and *S*-phase traveltime residuals of *PhaseNet* picks with regard to the 1-D velocity model from Diehl *et al.* (2009a) for the same event as in Fig. 4. Onsets selected and discarded by the *2-fit method* are marked by circles and diamonds, respectively, while stations without phase picks despite available waveform data are denoted with black dots.

Table 2. Overview of the workflow consisting of three subsequent inversion runs resulting in the final 1-D v_p and v_s models, hypocentral parameters x, y, z and t_{org} and station correction terms τ^P and τ^S.

#run	Model	v_p, v_s	x, y, z	t_{org}	τ^P, τ^S	#ev	Δ
run1		Free	Free	Free	Free	78	0–130 km
run2	*AlpsLocPS*	Fix	Free	Free	Free	384	0–130 km
run3	*GAR1D_PS*	Free	Fix	Free	Free	384	0–1000 km

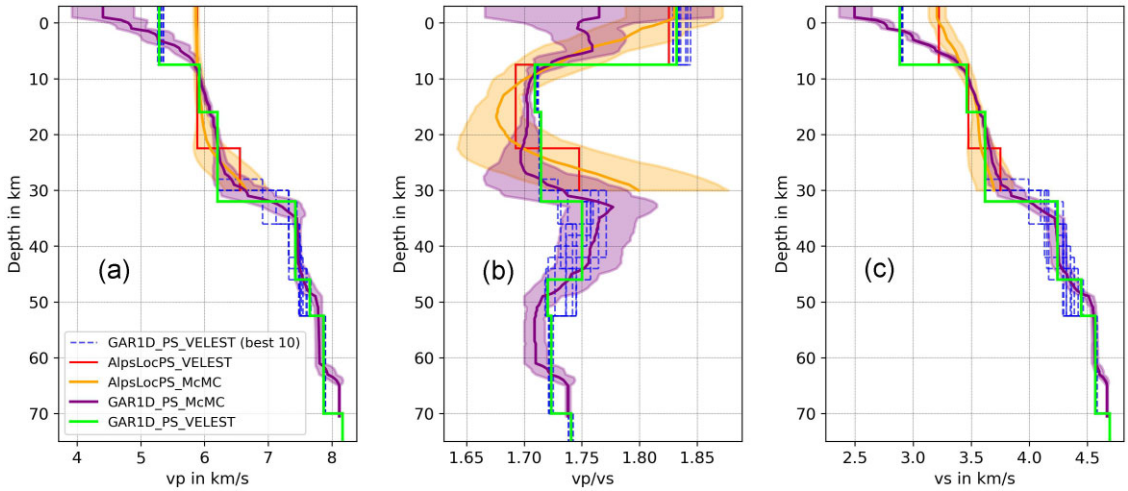

Figure 6. Comparison of the *AlpsLocPS_McMC* (orange), *AlpsLocPS_VELEST* (red), *GAR1D_PS_McMC* (purple) and the 10 best-fitting (blue, dashed) as well as the final best-fitting (lime) *GAR1D_PS_VELEST* 1-D velocity models. v_p, v_p/v_s and v_s distributions are plotted in panels (a), (b) and (c), respectively.

In the comparison of the derived v_p/v_s models (Fig. 6b) the largest discrepancy between all models again is present in the uppermost crust. For the remaining depth range the models are matching within their error margins with the highest uncertainty between 25 and 50 km depth.

Similar to v_p, the v_s structure of the McMC models (Fig. 6c) shows a gradual increase in the upper crust in contrast to the layered VELEST models with no systematic shift between the two, though. Below 10 km depth the models are matching very well with the highest uncertainty again between 25 and 50 km depth.

4.2 VELEST and McMC event locations and station corrections

Since the McMC algorithm is not given any initial hypocentres a comparison with the VELEST locations can be seen as a 'shift-test' which is commonly used to assess the dependency of final hypocentres from the initial locations. Resulting locations do not show a significant systematic shift and a horizontal and vertical scattering of $\sigma_{lat/lon} = 0.5$ km and $\sigma_{dep} = 2.3$ km, respectively (Fig. A10).

The final *P*- and *S*-phase station corrections τ^P and τ^S of the *GAR1D_PS_VELEST* model are displayed in Fig. 7 and show a smooth trend rather than unreasonable small scale oscillations.

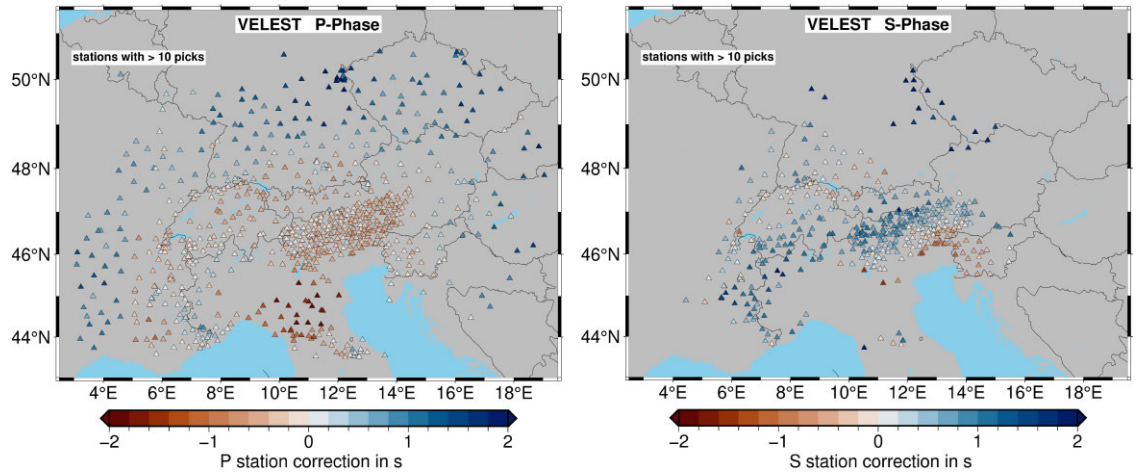

Figure 7. *P*- and *S*-phase station correction terms corresponding to the 1-D VELEST model based on observations from all distances.

They are in good agreement with station corrections of the *GAR1D_PS_McMC* (see Fig. A9). Minor differences can be attributed to the fact that VELEST computes station corrections relative to a reference station with $\tau^P = 0.0$ s whereas McMC has the boundary condition of a zero mean value of all values of $\tau^{P/S}$.

In summary, both VELEST and McMC models are explaining the data similarly well and velocities as well as hypocentres are coinciding well within the uncertainties.

4.3 Residual analysis

Fig. 8 shows the remaining *P*- and *S*-phase residuals corresponding to the final VELEST model for several epicentral distance ranges. *P*-phase residuals show a normal distribution around negligibly small mean values μ and increasing values of standard deviations σ with increasing distances Δ ranging from $\sigma = 0.42$ s ($\Delta = 0$–70 km) to $\sigma = 1.03$ s ($\Delta = 300$–1000 km). For $\Delta \geq 150$ km no significant increase of the residual with distance is observed. *S*-phase residuals at $\Delta \leq 150$ km also follow a standard distribution with only slightly increased values compared to *P* residuals. At $\Delta \geq 150$ km *S*-residuals are showing a increased standard deviation while being strongly reduced in the number of observations.

In the following we present polar diagrams of remaining *P*-phase residuals observed at single stations. Fig. 9(a) shows residuals for station VARN in NE Italy displayed over their distance and BAZ range. The distribution clearly clusters into a batch of predominantly negative residuals at $\Delta \leq 150$ km and another batch of predominantly positive residuals at $\Delta \geq 250$ km.

A comparable effect of BAZ dependent clusters can be seen in Fig. 9(b) displaying the remaining residuals of station WETR located in eastern Bavaria. While observations from the southwest show negative residuals throughout, for arrivals from the South positive residuals are obtained.

A special focus of this study lies on the inaccuracy of the automatic *PhaseNet* picks that are obtained in the crustal cross-over distance of *Pg*, *PmP* and *Pn* phases. Thus, we computed a set of 1-D VELEST models with varying layer boundaries for a catalogue including picks from all distances and for a catalogue excluding the distance range from 130 to 300 km. The 20 best-fitting models for both catalogues in Fig. A7 show, that adding picks from the cross-over distance mainly impacts the resulting velocity models in the lower crust, but does not introduce a significant shift towards systematically higher or lower velocities in either model.

We assessed the remaining residuals of picks from all distances corresponding to the best-fitting model computed when excluding the cross-over distance and find that picks in the cross-over distance do not show increased final residual values compared to observations from ≥300 km (see Fig. A8). Therefore, all following models we present contain observations from the entire epicentral distance range.

5 DISCUSSION

5.1 Static station corrections

We notice only mild variations of the *P* station corrections in the actual mountain range. In the contrary, larger variations of the *S*-station corrections are present, particularly in the SE we notice a prominent patch of negative station corrections. These match qualitatively with a region of elevated v_p/v_s ratio in the LET study by Jozi Najafabadi *et al.* (2022). As we include epicentral distances up to 1000 km in our *GAR1D_PS* model calculated station corrections (Fig. 7) are not only representing local site effects in the vicinity of each station but are systematically affected by large scale geological structures of the GAR such as Moho topography. Stations along the northern edge of the network in central Germany exclusively record phases from distances ≥200 km travelling updip along a southward dipping Moho (Spada *et al.* 2012) systematically reducing their traveltime. Therefore, static station corrections of ≈+2 s are most likely caused by Moho topography rather than local site effects. At stations with observations from near as well as far offsets such as station VARN in NE Italy a scalar station correction term is not sufficient to correct for distance-dependent residuals as illustrated in Fig. 9(a) leaving clusters of near and far observations with negative and positive remaining residuals, respectively. As Fig. 10 shows, this impact of *Pn*/*Sn* phases on the station corrections causes an increase of final residuals for *Pg* and *Sg* phases compared to their residuals after the relocation step where epicentral distances were limited to $\Delta_{max} = 130$ km. Although *Pg*-phase residuals are almost doubling from $\sigma = 0.25$ s to $\sigma = 0.46$ s the increase in *Sg*-phase residuals from $\sigma = 0.44$ s to $\sigma = 0.51$ s is less prominent due to the smaller number of *Sn* observations impacting the final *S* station corrections. This suggests that the final static station corrections are not adequate

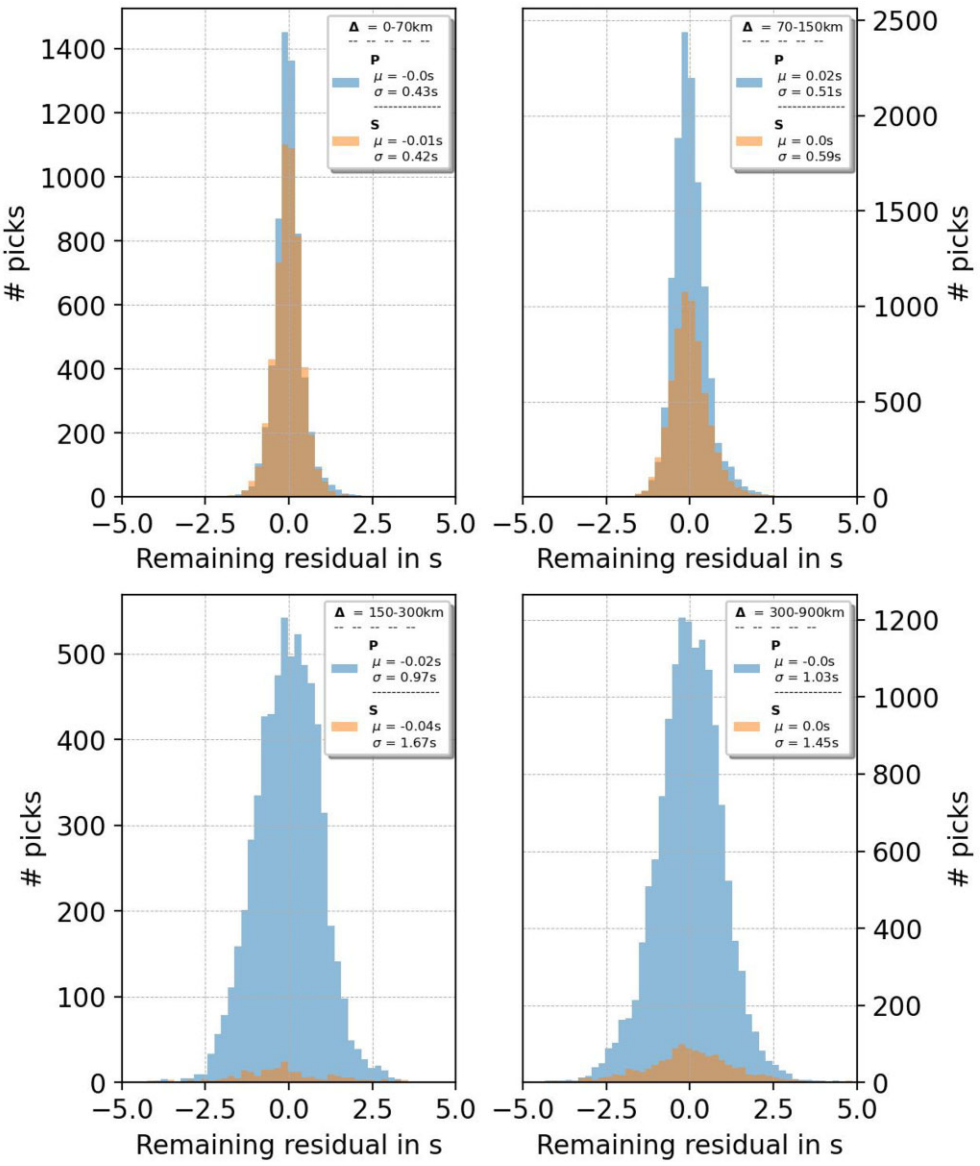

Figure 8. Distribution of remaining VELEST residuals for *P* phases (blue) and *S* phases (orange) observed within several epicentral distance ranges.

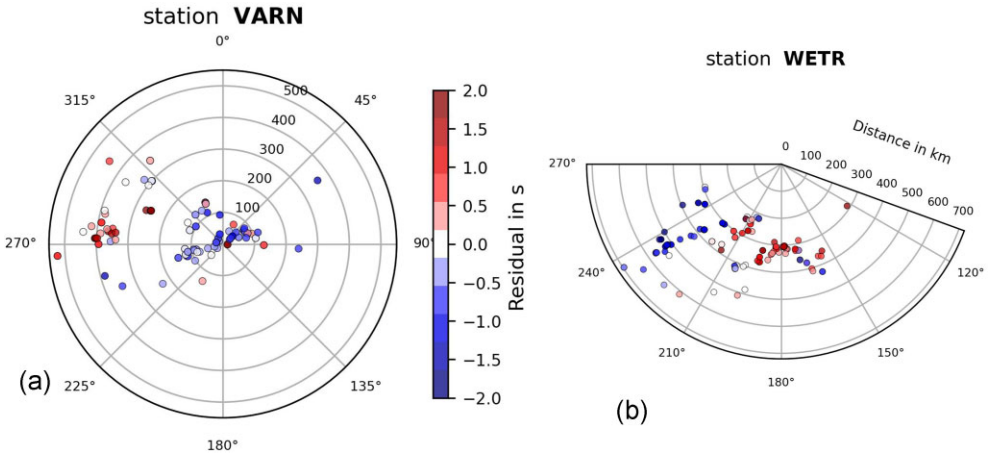

Figure 9. Polar diagrams illustrating the spatial distribution of the remaining VELEST *P*-phase residuals over BAZ and distance observed at the stations *VARN* (NE Italy) (a) and *WETR* (SE Germany) (b). Station locations are highlighted in Fig. 1.

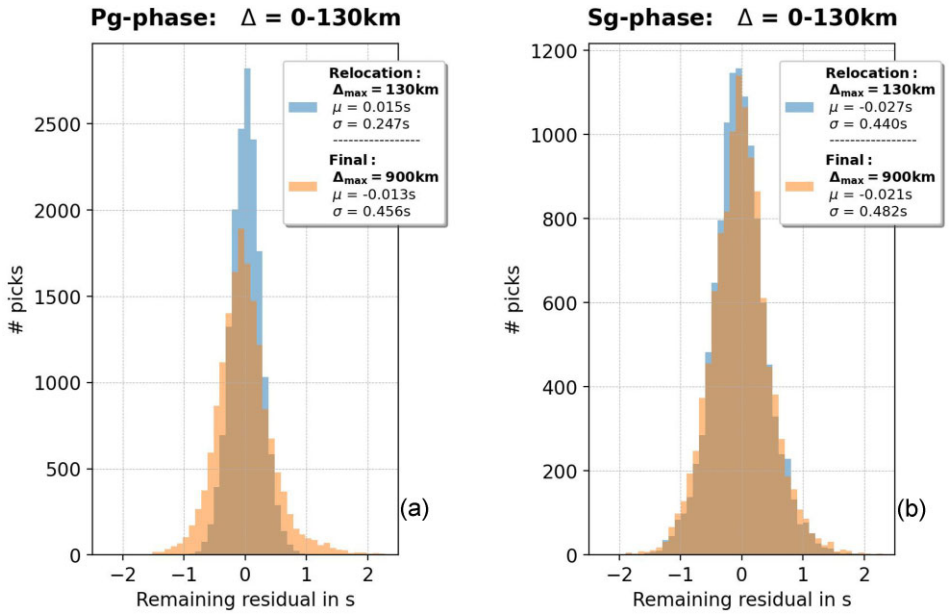

Figure 10. (a) *Pg*-phase residuals with regard to the model after the relocation step (blue) and after the final inversion run (orange). (b) *Sg*-phase residuals with regard to the model after the relocation step (blue) and after the final inversion run (orange).

to consistently correct for local site effects we recommend to use our intermediate model *AlpsLocPS* and its station corrections as published in the Supporting Information to locate seismicity within the GAR for *P* and *S* phases with epicentral distances $\leq$130 km. For events with a sufficient number of near observations, larger distances should not be considered anyway, due to the introduced increase of location uncertainty as shown by Diehl *et al.* (2021). In the following, we will compare our *AlpsLocPS* and *GAR1D_PS* models to previous studies of the region.

5.2 Comparison of 1-D velocity models

Fig. 11(a) shows the *GAR1D_PS_VELEST* (lime) and *GAR1D_PS_McMC* (purple) 1-D v_p models of this study in comparison with previous models from Bagagli *et al.* (2022) (blue), Diehl *et al.* (2021) (dark green) and Jozi Najafabadi *et al.* (2021) (cyan). The orogen wide model from Bagagli *et al.* (2022) is in good agreement with both our models showing no systematic offset and deviations due to different layering are mainly averaging out over depth. Generally, values of v_p are matching well between all models for the mid-crustal range between 10 and 20 km and are deviating slightly stronger above and below, which is consistent with the increased uncertainty of the McMC model in these depths. Deviations and increased uncertainties at shallow depths might be due to the high trade-off between station corrections and velocity values in the upper crust.

Similarly, the v_p/v_s ratio is well constrained for the mid-crustal range of 10–20 km depth as Fig. 11(b) demonstrates. Above and below this range the displayed v_p/v_s values are varying stronger. Fig. 11(c) compares the 1-D v_s models derived in this work with the smaller scale studies from Jozi Najafabadi *et al.* (2021) (cyan) & Diehl *et al.* (2021) (dark green) and selected 1-D profiles of 3-D *S*-wave velocity models obtained from ambient noise studies by Kästle *et al.* (2018) (blue) and Sadeghi Bagherabadi *et al.* (2021) (orange). The dashed, dotted and dash–dotted lines correspond to profiles from the Central Alps (46.85°N, 12.91°E), Po plain (45.05°N, 10.99°E) and Western Alps (45.85°N, 7.01°E), respectively, as marked in Fig. 1. Since these profiles are local representations of the velocity structure a detailed comparison with our models is not reasonable but represent the lateral variability in the GAR. The best agreement of all models is again visible in the mid-crust between 10 and 25 km depth followed by a range of increased deviation down to ≈45 km in accordance with the increased uncertainty of the *GAR1D_PS_McMC* model. As expected due to its thick sedimentary cover (Zuffetti & Bersezio 2021), the profile from the Po plain shows significantly lower shallow velocity values.

From the comparison above we conclude that the average velocity structure of the GAR is determined most consistently in the depth range between 10 and 25 km. For shallower depths model velocities are deviating stronger partially due to the high trade-off between velocity and station corrections which themselves greatly depend on the epicentral distance range selected. Receiver function studies (Spada *et al.* 2012; Mroczek & Tilmann 2021; Michailos *et al.* 2023) uniformly show large Moho topography ranging from 20 km in the northern Alpine foreland to more than 50 km beneath the Central Alps. As the substantial variations and uncertainties of the compared models within this depth range show, this large 3-D structure can not be captured in a 1-D model. Therefore, our models give a value of the average seismic velocities throughout the GAR. Below the maximum Moho depth of ≈55 km the models with sufficient resolution are in good agreement again.

Despite the mentioned issues, we present the first joined 1-D *P*- and *S*-wave velocity model and associated station corrections for the GAR based on seismic traveltimes. This will serve as input for subsequent high resolution 3-D tomographic study and provides consistent synthetic traveltimes, for example useful for removing outliers in the pick catalogue.

5.3 Comparison of hypocentres

In order to quantify the absolute accuracy of the determined event locations we compare our VELEST hypocentres to the results from

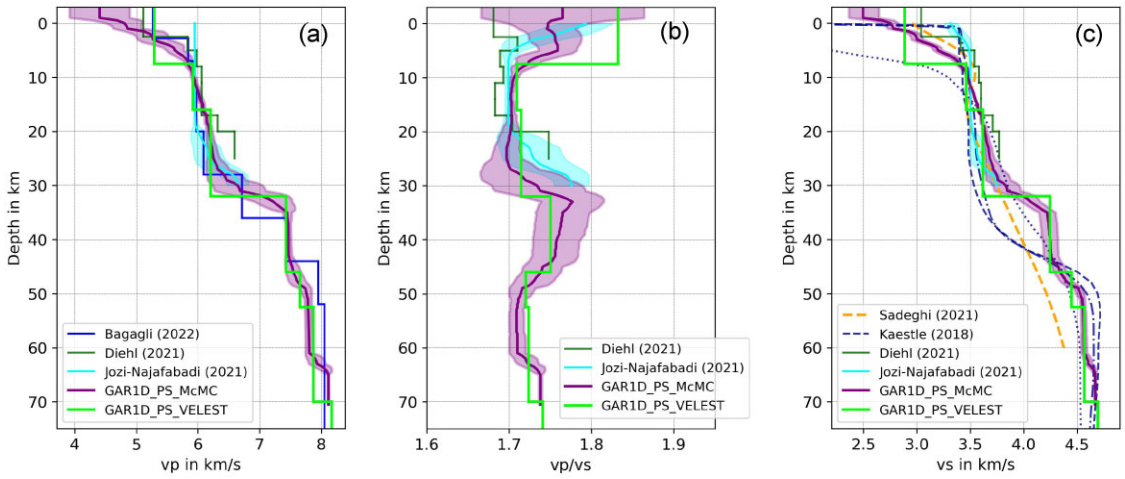

Figure 11. Compilation of our *GAR1D_VELEST* (lime) and *GAR1D_McMC* (purple) 1-D v_p, v_p/v_s and v_s models compared to results from previous studies within the GAR. (a) Comparison of our v_p models to the 1-D models from Bagagli *et al.* (2022) (blue), Diehl *et al.* (2021) (dark green) and Jozi Najafabadi *et al.* (2021) (cyan). (b) Comparison of our v_p/v_s models to Diehl *et al.* (2021)(dark green) and Jozi Najafabadi *et al.* (2021). (c) Comparison of our v_s models to Diehl *et al.* (2021) (dark green), Jozi Najafabadi *et al.* (2021) and selected 1-D v_s profiles from the 3-D ambient noise studies from Kästle *et al.* (2018) (darkblue) and Sadeghi Bagherabadi *et al.* (2021) (orange). The dashed, dotted and dash–dotted lines correspond to profiles from the Central Alps (46.85°N, 12.91°E), Po plain (45.05°N, 10.99°E) and Western Alps (45.85°N, 7.01°E), respectively.

Table 3. Comparison of deviations in event locations from Jozi Najafabadi *et al.* (2021), Bagagli *et al.* (2022) and our VELEST locations. For each pair of catalogues the number of matching events and the mean μ as well as the standard deviation σ for latitude, longitude and depth are listed.

	Jozi Najafabadi *et al.* (2021) versus Bagagli *et al.* (2022)	Jozi Najafabadi *et al.* (2021) versus VELEST this study	Bagagli *et al.* (2022) versus VELEST this study
#Events	106	40	307
σ_{lon} in km	2.1	1.5	1.3
μ_{lon} in km	−0.4	−0.2	−0.4
σ_{lat} in km	2.5	2.1	2.3
μ_{lat} in km	−0.6	−0.1	−0.7
σ_{dep} in km	6.1	5.8	6.3
μ_{dep} in km	−0.8	0.1	−0.1

Bagagli *et al.* (2022) and Jozi Najafabadi *et al.* (2021). A comparison of the 106 events matching between these two previous studies shows lateral variations of $\sigma_{\text{lat}} = 2.5$ km and $\sigma_{\text{lon}} = 2.1$ km with no significant systematic shift (Fig. A11). Event depth scatters stronger with $\sigma_{\text{dep}} = 6.1$ km. Table 3 gives an overview of variations in event locations from Bagagli *et al.* (2022), Jozi Najafabadi *et al.* (2021) and our VELEST model. Deviations throughout the three comparisons are quite consistent with values of $\sigma_{\text{lat}}/\sigma_{\text{lon}}$ between 1.3 and 2.5 km and σ_{dep} between 5.8 and 6.3 km. Comparing the final McMC locations to the previous studies yields very similar offsets.

This indicates that events in the GAR generally can be located with a horizontal accuracy of ≈2 km using a 1-D velocity model including station corrections. Hypocentral depths are varying by $\sigma \approx 6$ km between all catalogues and are not more consistent when including *S* phases as it has been done by Jozi Najafabadi *et al.* (2021) and this study. All referenced studies used their own picking methods and slightly different seismic stations which likely contributed to the rather large discrepancy in hypocentral depth. For more accurate event locations a denser station network and a consistent high resolution 3-D velocity model is required as, for example the local tomographic study of the Swiss region by Diehl *et al.* (2021) showed.

6 CONCLUSION

In this work, we present joined 1-D *P*- and *S*-wave velocity models including station corrections for the GAR based on seismic data from the *AlpArray Seismic Network* comprising more than 900 permanent and temporal seismic broad-band stations. We assess the performance of several state-of-the-art deep neural network picking algorithms with the Seismology Benchmark collection *SeisBench* and find *PhaseNet* to be the most suited for our data set, especially due to its high recall on the test data.

Comparison of pick probabilities attributed to each pick by *PhaseNet* with the manually assigned pick classes in a high precision reference catalogue show a clear correlation between *PhaseNet* probabilities and manual pick class as well as consistency of onset times of automatic and manual picks.

We developed a *2-fit-method* selecting picks based on their consistency in a data-driven way independently of *a priori* information such as an initial reference model. Choosing strict selection parameters allows us to consistently remove the overcritical *Pg*/*Sg* arrivals and thus include phases from the crustal cross-over distance increasing the resolution in the lower crust. Our final pick catalogue contains 18 820 *P*- and 12 005 *S*-arrivals observed at epicentral distances from 0 to 150 km and 20 781 *P*- and 1553 *S*-arrivals from 150 to 1000 km.

We demonstrate how distant observations can overprint the influence of local site effects in station correction terms when minimizing the final remaining residual at the cost of increasing the misfit for near observations. Therefore, we publish the 1D *P*- and *S*-wave model *AlpsLocPS* including station corrections based on picks with epicentral distances from $\Delta = 0$ to 130 km for consistent event localization throughout the entire GAR and a second model *GAR1D_PS* with data from $\Delta = 0$ to 1000 km resolving the entire crust and uppermost mantle allowing the computation of synthetic *P*- and *S*-phase traveltimes for the GAR.

A comparison of hypocentres determined in this work with locations of matching events from other studies shows epicentral uncertainties of $\sigma_{\text{lon/lat}} \approx 1.5$–$2.5$ km and variations in hypocentral depth of $\sigma_{\text{dep}} \approx 6.0$ km.

ACKNOWLEDGMENTS

We acknowledge the thoughtful advises from Tobias Diehl and Matteo Bagagli and thank them for their constructive feedback. We would like to thank the Deutsche Forschungsgemeinschaft (DFG) for funding this research with the grant numbers: RI 1089/2-1 and HA 3326/9-1. We acknowledge the Geophysical Instrument Pool Potsdam (GIPP) for providing the corresponding seismic stations. Map figures were created with GMT (Wessel *et al.* 2013) and PyGMT (Uieda *et al.* 2023) and the majority of seismic data processing was conducted using the ObsPy-Toolbox (Krischer *et al.* 2015).

The authors thank the AlpArray Seismic Network Team: György Hetényi, Rafael Abreu, Ivo Allegretti, Maria-Theresia Apoloner, Coralie Aubert, Simon Besançon, Maxime Bès de Berc, Götz Bokelmann, Didier Brunel, Marco Capello, Martina Čarman, Adriano Cavaliere, Jérôme Chèze, Claudio Chiarabba, John Clinton, Glenn Cougoulat, Wayne C. Crawford, Luigia Cristiano, Tibor Czifra, Ezio D'alema, Stefania Danesi, Romuald Daniel, Anke Dannowski, Iva Dasović, Anne Deschamps, Jean-Xavier Dessa, Cécile Doubre, Sven Egdorf, ETHZ-SED Electronics Lab, Tomislav Fiket, Kasper Fischer, Wolfgang Friederich, Florian Fuchs, Sigward Funke, Domenico Giardini, Aladino Govoni, Zoltán Gráczer, Gidera Gröschl, Stefan Heimers, Ben Heit, Davorka Herak, Marijan Herak, Johann Huber, Dejan Jarić, Petr Jedlička, Yan Jia, Hélène Jund, Edi Kissling, Stefan Klingen, Bernhard Klotz, Petr Kolínský, Heidrun Kopp, Michael Korn, Josef Kotek, Lothar Kühne, Krešo Kuk, Dietrich Lange, Jürgen Loos, Sara Lovati, Deny Malengros, Lucia Margheriti, Christophe Maron, Xavier Martin, Marco Massa, Francesco Mazzarini, Thomas Meier, Laurent Métral, Irene Molinari, Milena Moretti, Anna Nardi, Jurij Pahor, Anne Paul, Catherine Péquegnat, Daniel Petersen, Damiano Pesaresi, Davide Piccinini, Claudia Piromallo, Thomas Plenefisch, Jaroslava Plomerová, Silvia Pondrelli, Snježan Prevolnik, Roman Racine, Marc Régnier, Miriam Reiss, Joachim Ritter, Georg Rümpker, Simone Salimbeni, Marco Santulin, Werner Scherer, Sven Schippkus, Detlef Schulte-Kortnack, Vesna Šipka, Stefano Solarino, Daniele Spallarossa, Kathrin Spieker, Josip Stipčević, Angelo Strollo, Bálint Süle, Gyöngyvér Szanyi, Eszter Szücs, Christine Thomas, Martin Thorwart, Frederik Tilmann, Stefan Ueding, Massimiliano Vallocchia, Luděk Vecsey, René Voigt, Joachim Wassermann, Zoltán Wéber, Christian Weidle, Viktor Wesztergom, Gauthier Weyland, Stefan Wiemer, Felix Wolf, David Wolyniec, Thomas Zieke, Mladen Živčić and Helena Žlebčíková.

DATA AVAILABILITY

The *AlpsLocPS* and *GAR1D_PS* velocity models and corresponding station corrections are available at DOI:10.35097/1965. A catalogue of the relocated seismicity and all used arrival time picks is published there as well.

Event detections and initial locations were obtained from the European–Mediterranean Seismic Centre (EPOS-EMSC; *https://www.seismicportal.eu/*, last accessed 2023 July 25th). All seismic waveform data is publicly available and was accessed via the FDSN web service client for ObsPy (Krischer *et al.* 2015; last data download 2021 September 15). We used data from the following temporary and permanent seismic networks: BW [Department of Earth and Environmental Sciences, Geophysical Observatory, University of Munchen (2001)], CH [SED at ETH Zurich (1983)], CR [University of Zagreb (2001)], CZ [Charles University in Prague (Czech) *et al.* (1973)], FR [RESIF (1995)], GE [GEOFON Data Centre (1993)], GU [University of Genoa (1967)], HU [Kövesligethy Radó Seismological Observatory (Geodetic And Geophysical Institute, Research Centre For Astronomy And Earth Sciences, Hungarian Academy Of Sciences (MTA CSFK GGI KRSZO)) (1992)], IV [Istituto Nazionale di Geofisica e Vulcanologia (INGV) (2005)], MN [MedNet Project Partner Institutions (1988)], MT [French Landslide Observatory – Seismological Datacenter / RESIF (2006)], NI [OGS (Istituto Nazionale di Oceanografia e di Geofisica Sperimentale) and University of Trieste (2002)], OE [ZAMG – Zentralanstalt für Meterologie und Geodynamik (1987)], OX [Istituto Nazionale di Oceanografia e di Geofisica Sperimentale – OGS (2016)], PL, RD [RESIF (2018)], RF [University of Trieste (1993)], SI, SK [ESI SAS; Former GPI SAS (Geophysical Institute Of The Slovak Academy Of Sciences) (2004)], SL [Slovenian Environment Agency (1990)], ST [Geological Survey-Provincia Autonoma di Trento (1981)], YI [Chaljub (2017)], YW [Guéguen *et al.* (2017)], Z3 [AlpArray Seismic Network (2015)], ZS [Heit *et al.* (2017)], 1N [Malet *et al.* (2015)], 1P [Ritter *et al.* (2014)], 3C [Ohrnberger *et al.* (2023)], 4H, 8C [Helmstetter *et al.* (2020)], 8D [Swiss Seismological Service (SED) At ETH Zurich (2005)].

AUTHOR CONTRIBUTIONS

AR and CH planned and supervised the project. BB and AR developed the methodology and BB carried out the data processing. TR and BB adapted the McMC code accordingly. BB wrote the core of the paper. All authors contributed to the given interpretations and the final version of the paper.

CONFLICT OF INTEREST

The authors declare no conflicts of interest with respect to the research, authorship and publication of this paper.

SUPPORTING INFORMATION

Supplementary data are available at *GJIRAS* online.

Figure S1 Assessment of PhaseNet's performance when compared to the high quality manually determined *P*-phase arrival time catalogue from Diehl *et al.* (2009a).

Figure S1 (a) Comparison of *PhaseNet* and manually determined *P*- and *S*-phase arrival times from 30 events. (b) Comparison of *P*- and *S*-phase arrival times of 6 events independently picked by two human analysts.

Figure S3 Comparison of *PhaseNet* against manually determined *P*- and *S*-phase arrival times as in Fig. A2(a) for the epidistance ranges from 0 to 70 km (a), 70–150 km (b), 150–300 km (c) and 300–1000 km (d).

Figure S4 Assessment of *PhaseNet's* performance when compared to the manually revised *P*- and *S*-phase picks from Jozi Najafabadi *et al.* (2021).

Figure S5 Illustration of the 2-fit method to discard erroneous picks. *PhaseNet S*-phase arrivals are plotted over epicentral distance with a reduction velocity of 4.6 km s^{-1}. The corridor of considered picks is marked with green crosses at ±7 s around the synthetic onset (blue crosses). A linear regression is fit through the picks from 0 to 100 km and then extrapolated. All picks within the blue corridor at $\Delta \geq 150$ km within 4σ of this fit are labelled as overcritical *Sg* phases (cyan) and discarded. Later phases with $\Delta \geq 150$ km are discarded as *SmS*-arrivals (purple). A second weighted linear regression is fit through arrivals from 250–700 km and extrapolated until its interjection point with the first fit. Arrivals within 2σ of the fits plotted in red are selected, while the remaining picks marked in grey are discarded. In the case of more than one arrival on the same trace, only the first arrival within 2σ of the fit is considered. First and later arrivals on the same trace are marked with black and lime edgecolours, respectively.

Figure S6 Event section plots of the same event as in Figure 4(a) with manually determined *P*- and *S*-phase arrivals marked in red and green, respectively. (a) *Z*-component reduced by the approximate velocity of the direct *Pg* wave $v_{\mathrm{red}} = 6.0\,\mathrm{km\,s^{-1}}$. (b) *T*-component reduced by the approximate velocity of the *Sn* wave $v_{\mathrm{red}} = 4.6\,\mathrm{km\,s^{-1}}$.

Figure S7 Comparison of the the 20 best-fitting v_p (left-hand panel) and v_s (right-hand panel) VELEST models based on picks catalogues excluding (red) and including (blue) the cross-over range from 130 to 300 km.

Figure S8 Remaining *P*-phase residuals of observations from the entire epicentral range corresponding to the VELEST model which has been computed excluding picks from the cross-over distance range from 130 to 300 km.

Figure S9 *P*- and *S*-phase station correction terms corresponding to the *GAR1D_PS_McMC* model based on observations from all distances.

Figure S10 Differences in longitude and latitude (left-hand panel) and depth (right-hand panel) when comparing VELEST and McMC final event locations derived in this study.

Figure S11 Comparison of event locations from Bagagli *et al.* (2022) and Jozi Najafabadi *et al.* (2021). Horizontal and vertical discrepancies of epicentres are shown in the left- and right-hand panel, respectively.

Please note: Oxford University Press is not responsible for the content or functionality of any supporting materials supplied by the authors. Any queries (other than missing material) should be directed to the corresponding author for the paper.

REFERENCES

AlpArray Seismic Network, 2015. AlpArray Seismic Network (AASN) temporary component. Other/Seismic Network.. DOI:10.12686/ALPARRAY/Z3_2015.

Bagagli, M., Molinari, I., Diehl, T., Kissling, E. & Giardini, D., 2022. The alparray research seismicity-catalogue, *Geophys. J. Int.,* **231** . DOI:10.1093/gji/ggac226.

Chaljub, E., 2017. Saint-Guérin Arch Dam Experiment, 2015-2016, code YI, funded by chaire Pereniti (Grenoble INP, EDF), Université Grenoble Alpes, instrumented by RESIF-SISMOB. RESIF - Réseau Sismologique et géodésique Français. DOI: 10.15778/RESIF.YI2015.

Charles University in Prague (Czech), Institute of Geonics, Institute of Geophysics, Academy of Sciences of the Czech Republic, Institute of Physics of the Earth Masaryk University (Czech)& Institute of Rock Structure and Mechanics, 1973. Czech regional seismic network. DOI: 10.7914/SN/CZ.

Department of Earth and Environmental Sciences, Geophysical Observatory& University of Munchen, 2001. BayernNetz. DOI: 10.7914/SN/BW.

Diehl, T., Husen, S., Kissling, E. & Deichmann, N., 2009a. High-resolution 3-D P-wave model of the Alpine crust, *Geophys. J. Int.,* **179,** 1133–1147. DOI: 10.1111/j.1365-246X.2009.04331.x.

Diehl, T., Kissling, E., Husen, S. & Aldersons, F., 2009b. Consistent phase picking for regional tomography models: application to the greater Alpine region, *Geophys. J. Int.,* **176,** 542–554. DOI: 10.1111/j.1365-246X.2008.03985.x.

Diehl, T., Kissling, E., Herwegh, M. & Schmid, S., 2021. Improving absolute hypocenter accuracy with 3D Pg and Sg body–wave inversion procedures and application to earthquakes in the central Alps region, *J. geophys. Res.,* **126,** DOI:10.1029/2021JB022155.

ESI SAS; Former GPI SAS (Geophysical Institute Of The Slovak Academy Of Sciences), 2004. National network of seismic stations of Slovakia. DOI: 10.14470/FX099882.

French Landslide Observatory – Seismological Datacenter / RESIF, 2006. Observatoire Multi-disciplinaire des Instabilités de Versants (OMIV). DOI: 10.15778/RESIF.MT.

GEOFON Data Centre, 1993. GEOFON Seismic Network. DOI:10.14470/TR560404.

Geological Survey-Provincia Autonoma di Trento, 1981. Trentino seismic network. DOI: 10.7914/SN/ST.

Guéguen, P., Coutant, O. & Langlais, M.& RESIF, 2017. Maurienne seismic swarm 2017-2018. RESIF - Réseau Sismologique et géodésique Français. DOI: 10.15778/RESIF.YW2017.

Handy, M., Schmid, S., Bousquet, R., Kissling, E. & Bernoulli, D., 2010. Re-coiling plate-tectonic reconstructions of alpine tethys with the geological-geophysical record of spreading and subduction in the Alps, *Earth-Sci. Rev.,* **102,** 121–158. DOI: 10.1016/j.earscirev.2010.06.002.

Heit, B., Weber,, M., Tilmann,, F., Haberland,, C., Jia,, Y. & Pesaresi,, D. 2017. The swath-d seismic network in Italy and Austria. GFZ Data Services. DOI: 10.14470/MF7562601148.

Heit, B. *et al.*, 2021. The swath-d seismological network in the eastern Alps, *Seismol. Res. Lett.,* **92**(3), 1592–1609.

Helmstetter, A. & Guéguen, P.& RESIF, 2020. Seismic network 8C: monitoring swarms in the Mont-Blanc and Vallorcine area (RESIF - SISMOB). DOI: 10.15778/RESIF.8C2019.

Hetényi, G. *et al.*, 2018. The AlpArray seismic network: a large-scale european experiment to image the alpine orogen, *Surv. Geophys.,* **39,** DOI:10.1007/s10712-018-9472-4.

Istituto Nazionale di Geofisica e Vulcanologia (INGV), 2005. Rete sismica nazionale (RSN). Istituto Nazionale di Geofisica e Vulcanologia (INGV). DOI: 10.13127/SD/X0FXNH7QFY.

Istituto Nazionale di Oceanografia e di Geofisica Sperimentale - OGS, 2016. North-East Italy seismic network. FDSN. DOI: 10.7914/SN/OX.

Jozi Najafabadi, A., Haberland, C., Ryberg, T., Verwater, V., Le Breton, E., Handy, M., Weber, M. & Swath-D, A., 2021. Relocation of earthquakes in the southern and eastern Alps (Austria, Italy) recorded by the dense, temporary SWATH-D network using a Markov chain Monte Carlo inversion, *Solid Earth,* **12,** 1087–1109. DOI: 10.5194/se-12-1087-2021.

Jozi Najafabadi, A., Haberland, C., Le Breton, E., Handy, M., Verwater, V., Heit, B. & Weber, M., 2022. Constraints on crustal structure in the vicinity of the adriatic indenter (European Alps) from Vp and Vp / Vs local

earthquake tomography, *J. geophys. Res.,* **127,** DOI:10.1029/2021JB023160.
Kissling, E., Ellsworth, W., Eberhart-Phillips, D. & Kradolfer, U., 1994. Initial reference models in local earthquake tomography, *J. geophys. Res.,* **991,** 19 635–19 646. DOI: 10.1029/93JB03138.
Krischer, L., Megies, T., Barsch, R., Beyreuther, M., Lecocq, T., Caudron, C. & Wassermann, J., 2015. ObsPy: a bridge for seismology into the scientific Python ecosystem, *Comput. Sci. Discov.,* **8,** DOI:10.1088/1749-4699/8/1/014003.
Kästle, E., El-Sharkawy, A., Boschi, L., Meier, T., Rosenberg, C., Bellahsen, N., Cristiano, L. & Weidle, C., 2018. Surface wave tomography of the alps using ambient-noise and earthquake phase velocity measurements, *J. geophys. Res.,* **123,** DOI:10.1002/2017JB014698.
Kuang, W., Yuan, C. & Zhang, J., 2021. Real-time determination of earthquake focal mechanism via deep learning, *Nat. Commun.,* **12,** DOI:10.1038/s41467-021-21670-x.
Kövesligethy Radó Seismological Observatory (Geodetic and Geophysical Institute, Research Centre for Astronomy and Earth Sciences, Hungarian Academy of Sciences (MTA CSFK GGI KRSZO)), 1992. Hungarian national seismological network. GFZ Data Services. DOI: 10.14470/UH028726.
Lapins, S., Goitom, B., Kendall, J., Werner, M., Cashman, K. & Hammond, J., 2021. A little data goes a long way: automating seismic phase arrival picking at nabro volcano with transfer learning, *J. geophys. Res.,* **126,** DOI:10.1029/2021JB021910.
Lomax, A., Virieux, J., Volant, P. & Berge-Thierry, C., 2000. *Probabilistic Earthquake Location in 3D and Layered Models,* pp. 101–134, Springer Netherlands. DOI:10.1007/978-94-015-9536-0_5.
Malet, J.-P. *et al.*, 2015. French Landslide Observatory – OMIV (Temporary data) (MT-campagne) (RESIF - SISMOB). RESIF - Réseau Sismologique et géodésique Français. DOI: 10.15778/RESIF.1N2015.
MedNet Project Partner Institutions, 1990. Mediterranean Very Broadband Seismographic Network (MedNet). Istituto Nazionale di Geofisica e Vulcanologia (INGV). DOI: 10.13127/SD/fBBBtDtd6q.
Michailos, K. *et al.*, 2023. Moho depths beneath the European Alps: a homogeneously processed map and receiver functions database, *Earth Syst. Sci. Data,* **15,** 2117–2138. DOI: 10.5194/essd-15-2117-2023.
Michelini, A., Cianetti, S., Gaviano, S., Giunchi, C., Jozinović, D. & Lauciani, V., 2021. INSTANCE – the Italian seismic dataset for machine learning, *Earth Syst. Sci. Data,* **13**(12), 5509–5544.
Münchmeyer, J., Bindi, D., Leser, U. & Tilmann, F., 2021. Earthquake magnitude and location estimation from real time seismic waveforms with a transformer network, *Geophys. J. Int.,* **226**(2), 1086–1104.
Münchmeyer, J. *et al.*, 2022. Which picker fits my data? a quantitative evaluation of deep learning based seismic pickers, *J. geophys. Res.,* **127**(1), e2021JB023499, e2021JB023499 2021JB023499.
Mousavi, S., Sheng, Y., Weiqiang, Z. & Beroza, G., 2019. STanford EArthquake Dataset (STEAD): A Global Data Set of Seismic Signals for AI, *IEEE Access,* **7,** 179 464–179 476. DOI: 10.1109/ACCESS.2019.2947848.
Mousavi, S., Ellsworth, W., Weiqiang, Z., Chuang, L. & Beroza, G., 2020. Earthquake transformer–an attentive deep-learning model for simultaneous earthquake detection and phase picking, *Nat. Commun.,* **11,** 3952. DOI: 10.1038/s41467-020-17591-w.
Mroczek, S. & Tilmann, F., 2021. Joint ambient noise auto-correlation and receiver function analysis of the Moho, *Geophys. J. Int.,* **225,** DOI:10.1093/gji/ggab065.
NCEDC, 2014. Northern California Earthquake Data Center. Dataset. UC Berkeley Seismological Laboratory. DOI: 10.7932/NCEDC.
OGS (Istituto Nazionale di Oceanografia e di Geofisica Sperimentale) and University of Trieste, 2002. North-East Italy Broadband Network. International Federation of Digital Seismograph Networks. DOI: 10.7914/SN/NI.
Ohrnberger, M., Dahm, T., Krüger, F., Hannemann, K. & Korn, M., 2023. University of Potsdam Experimental 3D-3C Array. GFZ Data Services. DOI: 10.14470/1N671943.
RESIF, 1995. RESIF-RLBP French Broad-band network, RESIF-RAP strong motion network and other seismic stations in metropolitan France. RESIF - Réseau Sismologique et géodésique Français. DOI: 10.15778/RESIF.FR.
RESIF, 2018. CEA/DASE broad-band permanent network in metropolitan France. RESIF - Réseau Sismologique et géodésique Français. DOI: 10.15778/RESIF.RD.
Ritter, J. R. R., Schmidt, B., Haberland, C. & Weber, M., 2014. DEEP-TEE Phase 1. GFZ Data Services. DOI: 10.14470/6C709520.
Ross, Z. E., Meier, M., Hauksson, E. & Heaton, T. H., 2018. Generalized seismic phase detection with deep learning, *Bull. seism. Soc. Am.,* **108**(5A), 2894–2901. DOI:10.1785/0120180080.
Ryberg, T. & Haberland, C., 2019. Bayesian simultaneous inversion for local earthquake hypocentres and 1-D velocity structure using minimum prior knowledge, *Geophys. J. Int.,* **218**(2), 840–854.
Sadeghi Bagherabadi, A., Vuan, A., Aoudia, A., Parolai, S. & Group, T., 2021. High-resolution crustal S-wave velocity model and Moho geometry beneath the southeastern Alps: new insights from the SWATH-D experiment, *Front. Earth Sci.,* **9,** DOI:10.3389/feart.2021.641113.
SCEDC, 2013. Southern California Earthquake Data Center, CALTECH. Dataset. DOI: 10.7909/C3WD3xH1.
Schmid, S., Fügenschuh, B., Kissling, E. & Schuster, R., 2004. Tectonic map and overall architecture of the alpine orogen, *Eclog. Geol. Helvet.,* **97,** 93–117. DOI: 10.1007/s00015-004-1113-x.
Swiss Seismological Service (SED) At ETH Zurich, 1983. National seismic networks of Switzerland. ETH Zürich. DOI: 10.12686/sed/networks/ch.
Slovenian Environment Agency, 1990. Seismic network of the Republic of Slovenia. International Federation of Digital Seismograph Networks. DOI: 10.7914/SN/SL.
Spada, M., Bianchi, I., Kissling, E., Agostinetti, N. & Wiemer, S., 2012. Combining controlled-source seismology and receiver function information to derive 3-D Moho topography for Italy, *Geophys. J. Int.,* **194,** 1050–1068. DOI: 10.1093/gji/ggt148.
Swiss Seismological Service (SED) At ETH Zurich, 2005. Temporary deployments in Switzerland associated with aftershocks and other seismic sequences. ETH Zurich. DOI: 10.12686/sed/networks/8d.
Uieda, L. *et al.*, 2023. PyGMT: a python interface for the generic mapping tools. DOI: 10.5281/zenodo.3781524.
University of Genoa, 1967. Regional seismic network of north western Italy. International Federation of Digital Seismograph Networks. DOI: 10.7914/SN/GU.
University of Trieste, 1993. Friuli Venezia Giulia accelerometric network. International Federation of Digital Seismograph Networks. DOI: 10.7914/SN/RF.
University of Zagreb, 2001. Croatian seismograph network. International Federation of Digital Seismograph Networks. DOI: 10.7914/SN/CR.
Weiqiang, Z. & Beroza, G., 2018. PhaseNet: a deep-neural-network-based seismic arrival time picking method, *Geophys. J. Int.,* **216,** 261–273. DOI:10.1093/gji/ggy423.
Wessel, P., Smith, W. H. F., Scharroo, R., Luis, J. & Wobbe, F., 2013. Generic mapping tools: improved version released, *EOS, Trans. Am. geophys. Un.,* **94**(45), 409–410.
Woollam, J., Rietbrock, A., Bueno Rodriguez, A. & De Angelis, S., 2019. Convolutional neural network for seismic phase classification, performance demonstration over a local seismic network, *Seismol. Res. Lett.,* **90,** DOI:10.1785/0220180312.
Woollam, J. *et al.*, 2022. SeisBench–a toolbox for machine learning in seismology, *Seismol. Res. Lett.,* **93,** DOI:10.1785/0220210324.
ZAMG - Zentralanstalt für Meterologie und Geodynamik, 1987. Austrian seismic network. International Federation of Digital Seismograph Networks. DOI: 10.7914/SN/OE.
Zuffetti, C. & Bersezio, R., 2021. Space-time geological model of the quaternary syntectonic fill of a foreland basin (Po Basin, Northern Italy), *Sediment. Geol.,* **421,** DOI:10.1016/j.sedgeo.2021.105945.